



PCCP

Coordination and Thermophysical Properties of Select Trivalent Lanthanides in LiCl-KCl

| | |
|-------------------------------|---|
| Journal: | <i>Physical Chemistry Chemical Physics</i> |
| Manuscript ID | CP-ART-07-2021-003056.R3 |
| Article Type: | Paper |
| Date Submitted by the Author: | 15-Mar-2022 |
| Complete List of Authors: | Fuller, Jon; University of Nevada, Reno, Materials Science and Engineering Moon, Jeremy ; University of Nevada, Reno, Chemical and Materials Engineering Zhang, Jing; University of Nevada, Reno, Chemical and Materials Engineering Chidambaram, Dev; University of Nevada, Reno, Chemical & Materials Engineering Department An, Qi; University of Nevada, Reno, Chemical and Materials Engineering |
| | |

SCHOLARONE™
Manuscripts

Coordination and Thermophysical Properties of Select Trivalent Lanthanides in LiCl-KCl

Jon Fuller¹, Jeremy Moon¹, Jing Zhang¹, Dev Chidambaram¹ and Qi An^{1*}

¹ Department of Chemical and Materials Engineering, University of Nevada – Reno, Nevada 89577, United States

ABSTRACT

The coordination chemistry of various fission and decay products, such as actinides and lanthanides, are crucial to the commercial deployment of molten salt reactors as they can affect the thermophysical properties. Here, we examined the structure, coordination environment, physical properties such as density and the vibrational density of states for three lanthanide species, namely Ce, Eu, and Sm in LiCl-KCl eutectic system using the combination of quantum mechanics simulations and spectroscopic experiments. Quantum mechanics molecular dynamics (QM-MD) modelling was employed to determine the physical properties for each system resulting in accurate local coordination for each species. Then, the vibrational density of states (DOS) was determined using a two-phase thermodynamic modelling which was then compared to the experimentally obtained Raman spectra of the species in molten LiCl-KCl of eutectic composition. We find that Ce³⁺, Eu³⁺ and Sm³⁺ were all found to adopt octahedral local coordination environments in the eutectic salt composition in good agreement with experimental results. Ce³⁺ is found to fluctuate between an octahedral six-coordinated and a seven-coordinated structure due to the increased local proximity of Cl in the eutectic salt, resulting in a lower fluidicity/diffusivity than the other trivalent lanthanides studied. The thermophysical properties of the eutectic composition with trivalent lanthanides were not significantly different from the pure eutectic salt composition, but several changes were noted.

1. INTRODUCTION

The behavior of lanthanides in molten salt media has been an important area of focus for speciation research due to the role of lanthanides as fission products with important ramifications for both pyroprocessing¹ and efficient molten salt reactor (MSR) design.² Pyroprocessing is a promising process for treating spent nuclear fuel in an efficient manner, and drastically reduces the long-term storage requirements for spent nuclear fuel by effectively separating radioactive actinides from other fission products.³ Obtaining better understanding of the behavior of the other fission products, including decay chain products such as lanthanides, allows for more efficient pyroprocessing design.⁴ Similarly, the behavior of U and several of the primary actinide products from U fission have been well-researched in the past.⁵⁻⁷ The understanding of lanthanide behavior in relation to both systems is less clear, however.

Lighter lanthanides are formed in abundance during fission processes, with several specific species being of particular interest, including various isotopes of Ce which have relatively low half-lives but produce significant amounts of radiation through beta decay⁸ and

Sm which can cause reactor poisoning due to its ability to act as a neutron absorber. Particularly, the ^{149}Sm isotope is radioactively stable and results from the lanthanide decay chain in U fission.⁹ Another species of interest is Eu, which also can serve as a neutron poison in reactors¹⁰ but is of primary interest due to its high reactivity with other species commonly present in reactor and pyroprocessing systems. Understanding the speciation of all three of these lanthanides is of particular interest for MSR designs.

Lanthanides in LiCl-KCl are understood to typically form octahedral local coordination due to the +3 oxidation state dominating under typical conditions, and this has been observed in electrochemistry experiments with both oxides¹¹ and in the pure eutectic system¹² for various lanthanide species. An exception to this is Eu, which has been found to exist in both Eu^{2+} and Eu^{3+} in LiCl-KCl under temperatures elevated from typical pyroprocessing conditions.¹³ In the 3+ state, these lanthanides form octahedral chlorocomplexes in the eutectic salt composition; the six-coordinated structure is generally found to be relatively stable in LiCl-KCl and introduces unique considerations for efficient separation in pyroprocessing systems, since the lanthanides will typically prefer to remain in the salt rather than separate out.¹⁴ Likewise, this preference may provide an important clue for mitigating the buildup and neutron poisoning behavior of the fission product ^{149}Sm in reactors, which could increase overall reactor efficiency through improved design.

In the present study, we utilized quantum mechanics molecular dynamics (QM-MD) simulations to examine multiple relevant features of Sm^{3+} , Eu^{3+} and Ce^{3+} in the LiCl-KCl eutectic molten salt composition, including properties such as density, the vibrational density of states (DOS), and the coordination of each species in the molten chloride melt. We also present experimental measurements of these various properties and compare the calculated vibrational DOS with experimentally obtained Raman spectra for Sm^{3+} and Eu^{3+} . We find good agreement between our computational models and the experimental data, validating these computational methods for predicting the local coordination of lanthanide species in LiCl-KCl as well as important thermophysical properties that may influence more efficient reactor and pyroprocessing technique design in the future. These computational and experimental methods can be extended to various other salt systems to provide insight into the behavior of lanthanides or other species in a similar manner to the work presented here.

2. COMPUTATIONAL AND EXPERIMENTAL METHODS

2.1 QM-MD Simulations

All QM-MD results reported here utilize the Perdew-Burke-Ernzerhof (PBE)^{15,16} functional of Density Functional Theory employing the D3 (Grimme)¹⁷ corrections for van der Waals long-range interactions. All calculations were performed using the VASP¹⁸⁻²⁰ software package with plane wave basis set. The Langevin thermostat and barostat were used to control the temperature and pressure in the molecular dynamics (MD) simulations with the isobaric-isothermic (NPT) ensemble applied to obtain the equilibrium structures at various temperatures. An energy cutoff of 400 eV was specified for all calculations, with a convergence criterion for

SCF energy specified as 1.0×10^{-4} eV. The sampling in the Brillouin-zone was performed with the Γ -point only. Fermi smearing was used in all calculations for this work.

A supercell designed to mimic the LiCl-KCl eutectic composition of 59.2% mol LiCl comprised of 36 Li, 64 Cl and 25 K atoms as well as a single lanthanide ion was created to result in an appropriate wt. % for each lanthanide-chloride specie to match the experimental composition in each case. Additionally, for the Ce^{3+} case a higher wt. % (19.7 %) was prepared using three Ce^{3+} atoms in a system comprised of 32 Li, 64 Cl, and 23 K atoms was also evaluated to better match experimental results. Equilibrium liquid structure was achieved for each atomic species initially by high-temperature (2000 K) QM-MD well above the melting point for the salt. Then, the structure in each case was taken through a rapid quenching process (5 ps) to 773 K, the typical operating temperature of pyroprocessing systems, and then equilibrated at this temperature for a minimum of 10 ps in order to find an energy converged system at zero pressure. NPT dynamics (allowing the volume to change in order to find the density of the system) were then performed on this system iteratively (for a minimum of 20 ps) until the energy and volume of the system converged to an appropriate value. Using the equilibrium structure from NPT, the NVT dynamics were then performed (again for a minimum of 20 ps) in order to obtain the trajectory for two-phase thermodynamic analysis discussed below.

2.2 Simulation Analysis Techniques

The volume of the cell for each individual position in the final 10 ps of each NPT dynamics simulation was calculated based on the reported cell parameters, then divided by the number of ions in the system to find the per-ion volume. This per-ion volume was then combined with the total mass of all atoms in the system to find the density of the composition. The radial distribution function (RDF), $g(r)$, are calculated for each pair and the total system using the standard method²¹ utilizing the atomic positions in the MD trajectories. The coordination number (CN) are then obtained from the integration of RDFs.

2.3 2PT Analysis / Green-Kubo Formalism

In order to evaluate the thermophysical properties and calculate the vibrational density of states for the liquid-phase molten salt system, a two-phase thermodynamic model was employed in which the vibrational DOS (obtained by performing a Fourier transform on the velocity autocorrelation functions (VAFs) in the QM-MD trajectory in 20 picosecond segments) is analyzed in terms of both configurational and vibrational modes as two distinct components: a gas (diffusive) component with modes at zero frequency and scaling damping applied to higher modes and a solid (non-diffusive) component with no states at zero frequency. A quantum statistics approach is applied to the solid component to obtain thermodynamic properties and a hard sphere thermodynamics model is applied to the gas component to obtain thermodynamic properties. These two thermodynamic ‘partitions’ are then averaged together to determine the liquid-phase vibrational DOS appropriate for the molten salt systems. The accurate thermophysical properties can be obtained from the 2PT method using the short MD trajectory (20 ps). This method is well-described in previous works.²²⁻²⁴

Various thermodynamic and transport properties are derived using the Green-Kubo formalism from the VAFs obtained from the QM-MD trajectory. The diffusion of the system represents the movement of atoms in materials relating to phase change as a kinetic process. To obtain the diffusion constant, or diffusivity, the VAFs are integrated according to the Green-Kubo equation:

$$D = \frac{1}{3} \int_0^{\infty} \text{VAF}(t) dt \quad (1)$$

The fluidicity, also known as the reciprocal of viscosity, measures the ease of flow of the fluid phase of a substance. The viscosity of the substance is obtained using the Green-Kubo formalism using the shear stress autocorrelation function obtained from QM-MD from the equation:

$$\eta = \frac{\Omega}{k_B T} \int_0^{\infty} \Pi^{\alpha\beta}(t) \Pi^{\alpha\beta}(0) dt \quad (2)$$

where $\Pi^{\alpha\beta}(t)$ represents the portion of the stress tensor ($\alpha \neq \beta$), k_B represents the Boltzmann constant, T represents temperature in K, and Ω represents volume. The reciprocal of the viscosity is taken to obtain the fluidicity of the molten salt systems described in this work.

2.4 Experimental Apparatus

A 532 nm, 300W laser was used as the excitation source for Raman scattering. The incident light and Raman scattered light were transported to and from the melt using a custom fabricated fiber optic cable and optics. The optics contain focal lenses in addition to polarization filters to facilitate perpendicular and parallel polarization analysis. The iHR320 Imaging Spectrometer (Horiba) with a Syncerity Charge-Coupled Device (CCD) Deep Cooled Camera was used to record the Raman spectra. The effects of black body radiation on the Raman spectra were found to be minimal and were corrected through baselining studied samples against a blank under the same conditions. Details of this setup have been provided elsewhere.²⁵

2.5 Experimental Salt Composition

The fused salt mixtures from which the experimental Raman spectra were obtained consisted of a 46-54 wt.% eutectic mixture of lithium chloride (Alpha Aesar, 99.9% purity) and potassium chloride (KCl, Acros Organics, extra pure) dried overnight at 250 °C under vacuum and subsequently at 300 °C for 2h prior to melting in an Ar-atmosphere glovebox (<1ppm O₂, <0.5ppm H₂O) in which all subsequent steps were also carried out. Analyte salt was added to the eutectic LiCl-KCl salt mixture after fusion. Analytes were either SmCl₃ (Alpha Aesar anhydrous 99.9% pure or EuCl₃ (Alpha Aesar ultra-dry 99.99% pure) and comprised 5 wt.% of the total melt mass for SmCl₃ and EuCl₃. All melts were contained in a graphite crucible and heated using a ceramic resistance furnace controlled by a PID temperature controller (Watlow). Melt temperature was determined using K-type thermocouple immersed in the fused salt.

3. RESULTS AND DISCUSSION

3.1 Coordination of Species

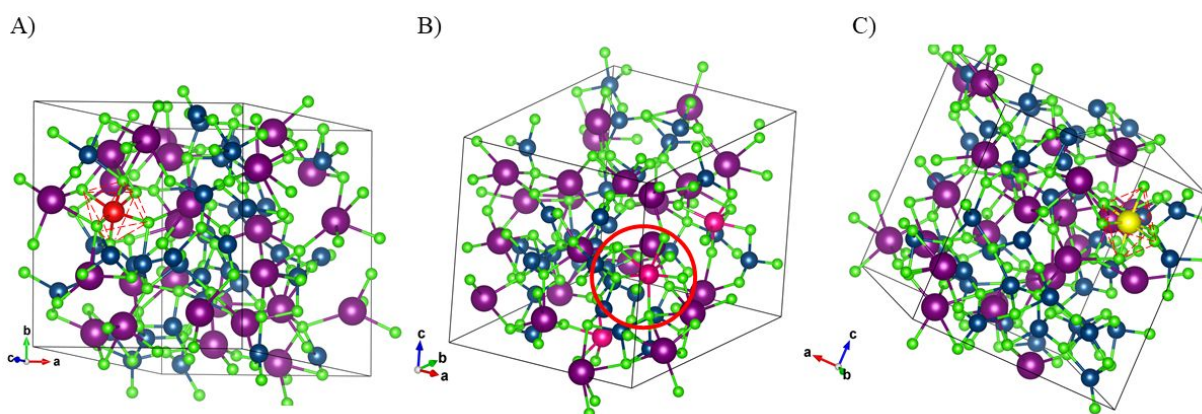


Fig. 1 – QM-MD-obtained preferred coordination of trivalent Sm in red (A), Ce in magenta (B) and Eu in yellow (C). Li, Cl and K atoms are shown in dark blue, green and purple, respectively. The octahedral SmCl_6^{3-} and EuCl_6^{3-} structures in (A) and (C) are shown with dashed red lines to indicate the geometry of the chlorocomplexes. 19.4 wt. % Ce (3 Ce atoms) is shown in (B), with a circled seven-coordinated chlorocomplex in the center. The coordination of 6.9 wt. % Ce (1 Ce atom) is shown in Fig. S1.

The behavior of trivalent lanthanides in LiCl-KCl eutectic has been mostly noted to tend towards six-coordinated octahedral structures in both experimental²⁶ and computational studies.^{27,28} Some discrepancies are found in specific trivalent species, such as Ce^{3+} , and are believed to be due to distortions in the octahedral structure arising from the lower stability of the resulting chlorocomplexes in pure LiCl-KCl compared to the other trivalent lanthanide species.²⁶ These distortions tend to result in a fluctuation between five, six, and seven coordinated structures due to changes in the proximity of constituent salt atoms to the lanthanide, influencing the local charge state.

The computationally determined coordination of Sm^{3+} is found to be octahedral six-coordinated SmCl_6^{3-} , in good agreement with previously reported data.²⁶ Bond angle distortion is found to be minimal for SmCl_6^{3-} compared to the other two species investigated, and it is the most stable species with minor fluctuations between five and six-coordinated structures observed during the NPT dynamics. The SmCl_6^{3-} chlorocomplex in LiCl-KCl is shown in Figure 1 (a) above. Similarly, Ce^{3+} is observed to form the octahedral six-coordinated CeCl_6^{3-} in the well-equilibrated system at both studied concentrations. Notable fluctuations are observed between a six and seven-coordinated system during NPT dynamics, with the system predominantly in the octahedral coordination. This behavior is noted as consistent between the 6.9 wt.% and 19.4 wt.% systems that we evaluated computationally. This fluctuation results in closer Cl to the Ce^{3+} ion, which produces a noticeable deviation from the expected RDF for the other trivalent lanthanides studied, which is described later in this section. This behavior is consistent from previous studies on both La^{3+} and Ce^{3+} .²⁶ The single CeCl_6^{3-} octahedral chlorocomplex is shown in Figure 1 (b) above. The Eu^{3+} cation likewise forms the octahedral EuCl_6^{3-} similar to the

expected behavior of other lanthanides in the LiCl-KCl medium.^{26,27} This octahedral behaves similarly to the Sm chloro complex reported above, with minimal deviation from a strong six-coordinated structure. The EuCl_6^{3-} chloro complex is shown in Figure 1(c) above.

Structural analysis

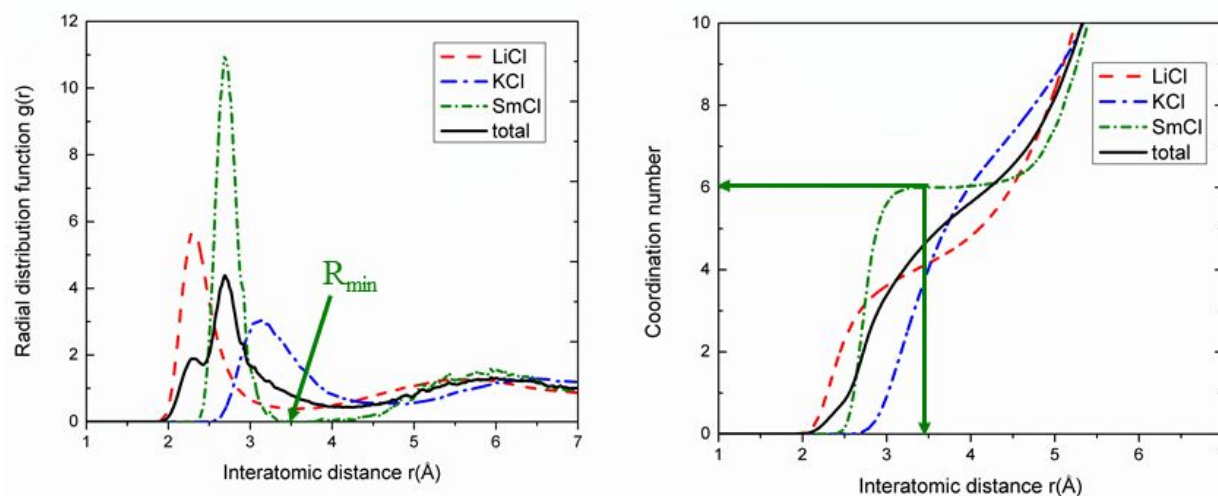


Fig. 2 – Radial distribution function $g(r)$ (left) and coordination number (right) for Sm^{3+} (SmCl_6^{3-}) in LiCl-KCl eutectic composition at 500°C. Li^+ , K^+ , and Sm^{3+} are represented by dashed red, blue and green lines, respectively, while the average total values of RDF and CN for Sm^{3+} are represented by a black line. R_{min} and CN are indicated with green arrows for clarity.

RDF analysis of Sm^{3+} in LiCl-KCl (shown in Figure 2) was performed for each species pair found in the composition. From the RDF the coordination number of each species pair was obtained to be 4.3, 7.1 and 6.0 for Li^+ , K^+ and Sm^{3+} in this system, respectively. The flatness of the Sm^{3+} coordination number curve indicates that a strong six-coordinated octahedral structure is prevalent, which is also observable in the MD trajectory for this species. Indeed, we find that the $\text{SmCl}_6^{(3-)}$ chloro complex is extremely stable in the MD, with very little fluctuation between either 5- or 7- coordinated states, which are frequently observed in the trivalent Ce system and less often in the trivalent Eu system.

Unlike Sm^{3+} , Ce^{3+} was found to reduce Li^+ and K^+ coordination numbers (4.1 and 6.8, respectively) in LiCl-KCl but a higher lanthanide-chloride coordination number for Ce^{3+} of 6.9. Experimentally, Ce^{3+} has been found to have a CN of ~ 6.52 in the pure CeCl_3 system.²⁸ However, other computational analyses of Ce^{3+} in LiCl-KCl have indicated a steady CN of ~ 6.9 similar to our own findings.²⁹ This discrepancy in CN is believed to be due to a stronger Ce-Cl interaction in Li-K-Cl systems compared to the interaction in the pure CeCl_3 system. This is likely caused by local charge differences causing a stronger interaction for Cl with the larger Ce^{3+} cation compared to the monovalent cations in the molten salt. This results in Cl clustering closer around the Ce^{3+} species, leading to a fluctuation between six and seven-coordinated for the chloro complex as noted previously. The RDF and CN behavior of 6.9 wt. % Ce^{3+} in LiCl-KCl is illustrated in Figure 3, while the RDF and CN behavior of 19.4 wt.% are shown in Figure

S2 of the SI. We see that the CN of Ce^{3+} decreases to ~ 6.6 in the higher wt. % system, which indicates a shift towards more rigorous octahedral coordination. This decrease in Ce-Cl attractivity as the amount of Ce^{3+} cations present in the system increases helps explain the change in thermophysical behavior, particularly fluidicity and diffusivity, which both increase significantly in the higher wt. % case (as shown in Table 1.) Since Cl is found to be not as tightly bound in the chlorocomplex at higher wt. %, the overall diffusivity of the system is more relaxed and thus found to be more similar to the low wt. % cases of the other two trivalent lanthanides studied here. Thus, we believe the stronger Ce-Cl interaction in the LiCl-KCl eutectic is offset at higher wt. % by increased repulsion between the CeCl_x chlorocomplexes and the non-neutral charge states, creating a more homogenous and less tightly clustered system.

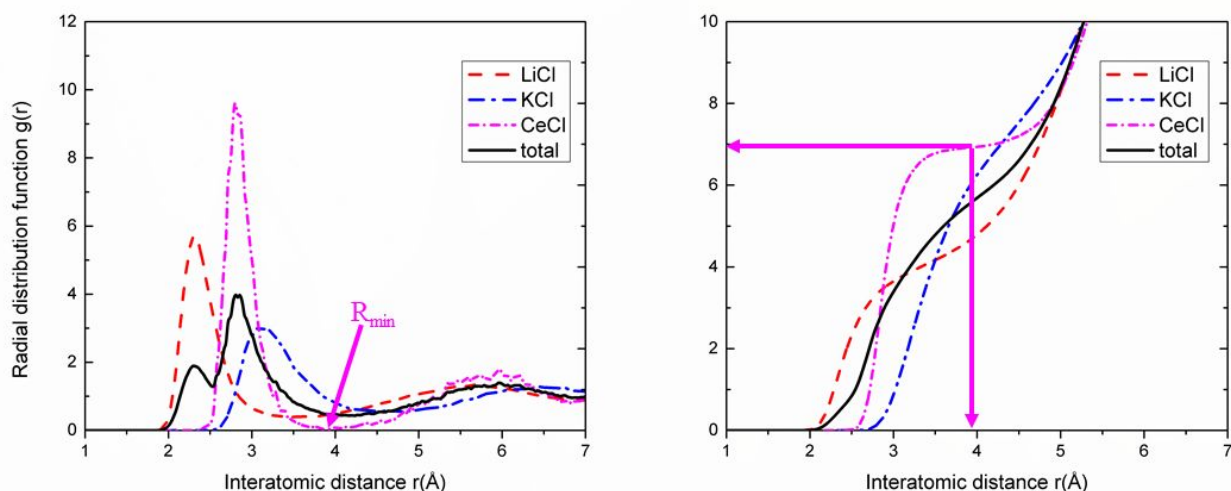


Fig. 3 - Radial distribution function $g(r)$ (left) and coordination number (right) for Ce^{3+} (CeCl_6^{3-}) (6.9 wt. %) in LiCl-KCl eutectic composition at 500°C. Li^+ , K^+ , and Ce^{3+} are represented by dashed red, blue and magenta lines, respectively, while the average total values of RDF and CN are represented by a black line. R_{\min} and CN for Ce^{3+} are indicated with magenta arrows for clarity. The corresponding data for high wt. % (19.4%) is found in Fig. S2.

Similarly, RDF/CN analysis of Eu^{3+} in LiCl-KCl was performed and indicates similar behavior for the trivalent lanthanide such as that found for Sm^{3+} . Coordination numbers of 4.1, 7.2 and 6.0 were found for Li^+ , K^+ , and Eu^{3+} (shown in Figure 4) in this system. This indicates a strong six-coordinated chlorocomplex, which was also evident in molecular dynamics. Eu^{3+} was found to have a similar effect on the Li^+ and K^+ coordination numbers as Sm^{3+} , indicating no significant change to Cl behavior in the system such as what was found for Ce^{3+} . This strongly coordinated behavior was also observed through the rigid octahedral coordination for Eu^{3+} in the molecular dynamics simulation with little fluctuation between other coordination states, although relatively rare fluctuations to a seven-coordinated state similar to that observed in the Ce systems was found at certain intervals in the MD.

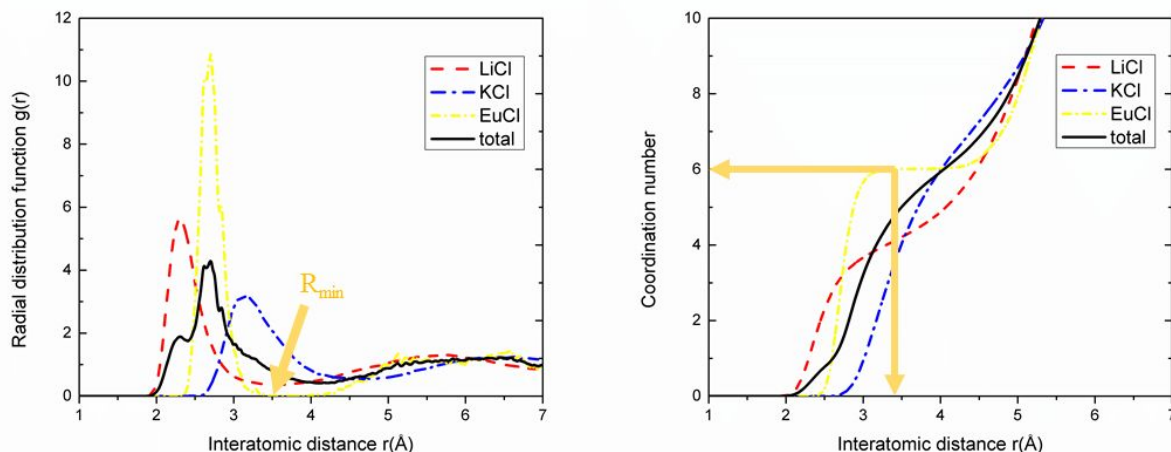


Fig. 4 - Radial distribution function $g(r)$ (left) and coordination number (right) for Eu^{3+} (EuCl_6^{3-}) in LiCl-KCl eutectic composition at 500°C . The Li^+ , K^+ , and Eu^{3+} RDF and CN are represented by dashed red, blue and magenta lines, respectively, while the average total values of RDF and CN are represented by a black line. R_{\min} and CN for Eu^{3+} are indicated with gold arrows for clarity.

3.2 Thermophysical Properties

Table 1 – Calculated properties of studied trivalent lanthanides from QM-MD and two-phase analysis of MD trajectories at 500°C . The calculated density agrees well with experimentally reported densities for Ce in LiCl-KCl eutectic.³¹

| Species (wt. %) | Calculated Density (g/cm^3) | Experimental Density (g/cm^3) | Specific Heat Capacity (C_v) ($\text{J}/\text{mol}\cdot\text{K}$) | Fluidicity | Diffusivity (cm^2/s) |
|--------------------------|---|---|---|------------|--|
| Pure LiCl-KCl | 1.606 | 1.621 | 22.30 | 0.205 | 2.40×10^{-5} |
| Sm^{3+} (7.4%) | 1.621 | - | 22.63 | 0.138 | 1.126×10^{-5} |
| Ce^{3+} (6.9%) | 1.668 | 1.676 | 23.09 | 0.097 | 5.656×10^{-6} |
| Ce^{3+} (19.4%) | 1.723 | 1.790 | 21.75 | 0.151 | 1.297×10^{-5} |
| Eu^{3+} (7.8%) | 1.619 | - | 22.65 | 0.134 | 1.038×10^{-5} |

Experimental density data was available only for the Ce^{3+} species in eutectic LiCl-KCl at various concentrations,³¹ from which values were extrapolated for comparing to our computational models. These are shown in the experimental density column of Table 1 above;

we find excellent agreement at low wt.% (6.9%) within $\sim 0.5\%$ of the experimental value and increasing deviation at higher wt.% (19.4%) for Ce^{3+} but still with good agreement within $\sim 4\%$ of the experimental value. This deviation at increasing wt.% is likely due to inadequacies within the computational model for treating the system containing multiple lanthanide cations. From the solid relation established between our Ce^{3+} model and the experimental density, we can thus verify consistent behavior for the other two lanthanide species studied using the same methods, Sm^{3+} and Eu^{3+} at similar wt.% to the low-concentration Ce^{3+} species which do not have well-verified experimental density data available. As is expected, the density of all salt compositions containing trivalent lanthanides is increased compared to the pure salt at the studied temperature (500°C). We find slight increases in the specific heat capacity (C_v) for these compositions compared to the pure eutectic as well as a decrease in both fluidicity and diffusivity. This indicates that chlorocomplex formation around trivalent lanthanides inhibits both of these transport parameters in a significant manner at typical operating temperatures for the LiCl-KCl molten salt, while the specific heat capacity is not significantly altered by the inclusion of the lanthanide species.

Of particular interest in our evaluation of the physical properties of these species in molten LiCl-KCl eutectic using 2PT analysis is the lower fluidicity and diffusivity of 6.9 wt.% Ce^{3+} in LiCl-KCl which is significantly decreased compared to that of 7.4 wt.% Sm^{3+} in LiCl-KCl and 7.8% Eu^{3+} in LiCl-KCl; we believe this to be due to the closer clustering of Cl around Ce^{3+} causing the six-to-seven coordinated fluctuations which in turn also inhibits the configuration changes, leading to smaller diffusivity and fluidicity. Higher wt.% Ce^{3+} (19.4%) in LiCl-KCl has increased fluidicity and diffusivity more in line with the behavior of low wt.% Sm^{3+} and Eu^{3+} . This may arise from the repulsion of the CeCl_x clusters with non-neutral charged states. This behavior is detailed in section 3.1.

3.3 Vibrational DOS/ Raman

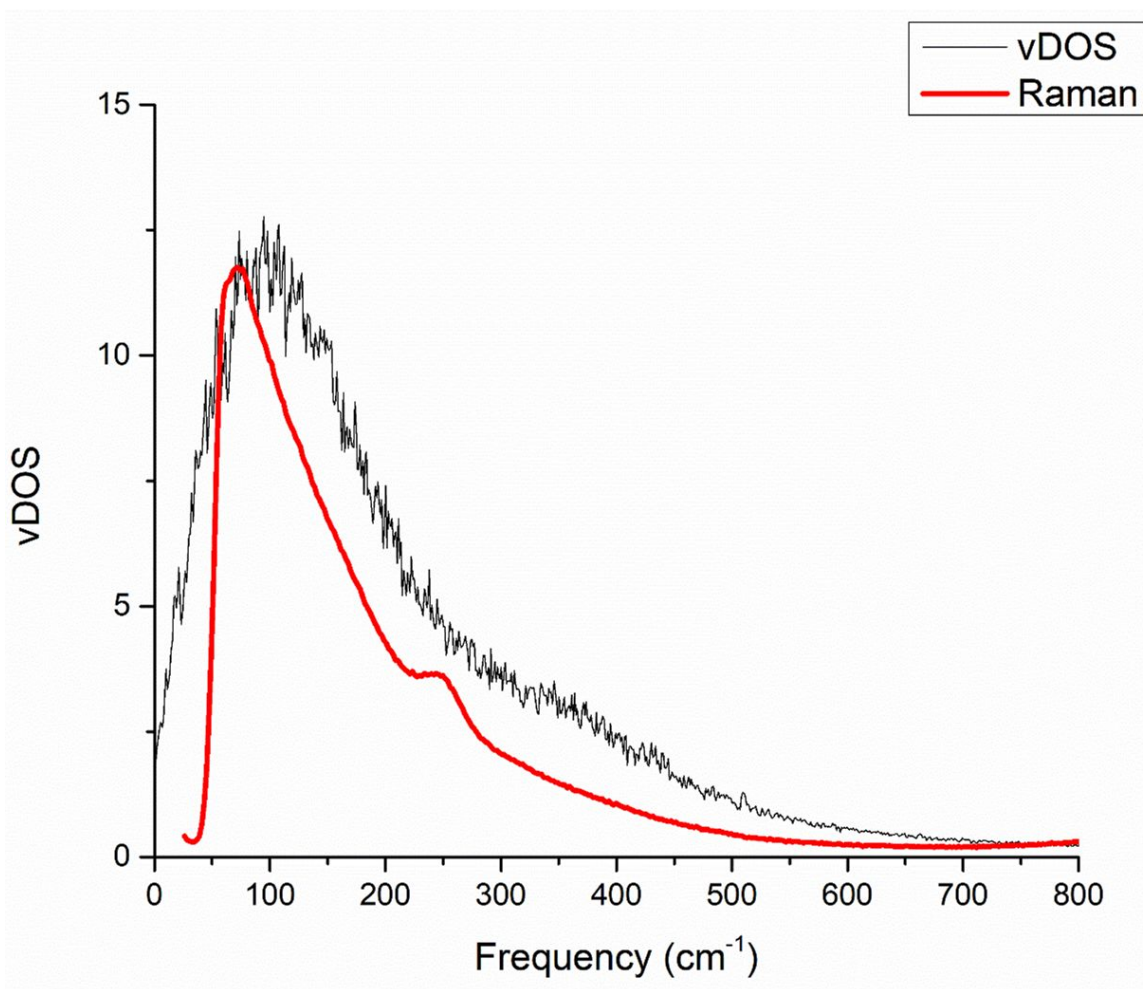


Fig. 5 - Vibrational DOS (black) and experimental Raman spectra (red) of Sm^{3+} (SmCl_6^{3-}) in LiCl-KCl at 500°C . The computational vibrational DOS is redshifted by $\sim 10\text{-}50\text{ cm}^{-1}$ compared to the experimentally obtained Raman spectrum (intensity of Raman scaled for comparison).

The vibrational density of states (vDOS) was obtained from the 2PT methodology by applying a Fourier transform to the relevant velocity autocorrelation function for both a non-diffusive solid component and diffusive gas component as previously described, which are then averaged together to obtain the vDOS for the liquid phase studied here.²² Raman spectroscopy study of metals in molten salts has been performed for decades to obtain useful insight into the coordination and behavior of chlorocomplexes in salt system.³² Raman spectroscopy as an analytical tool for determining the coordination of chlorocomplexes in molten salts has been performed with good results, including in complex multi-phase systems across various temperatures.³³ Since the intensity of Raman modes do not directly correspond to the intensity of the vibrational density of states due to the selection rules and various other considerations in complex systems,³⁴⁻³⁶ a general similarity in the vDOS and Raman modes can be assumed with differences in intensity across the spectrum. Due to the approximation nature of the 2PT calculation method, the vDOS of the studied lanthanide species in eutectic LiCl-KCl is broadly similar with minor yet recognizable differences. The vDOS of the blank LiCl-KCl eutectic salt

composition at 500°C is found in Fig. S3 of the SI for comparison with the presented results here. In Fig. 5 we note a main Raman peak at $\sim 90 \text{ cm}^{-1}$ with a secondary shoulder peak at $\sim 250 \text{ cm}^{-1}$; both have reasonable agreement with our computationally-obtained vDOS which has a broader single-peak primary feature between $\sim 50 \text{ cm}^{-1}$ and $\sim 150 \text{ cm}^{-1}$ with the highest vDOS at $\sim 105 \text{ cm}^{-1}$ with a slight uptick of a secondary feature at $\sim 260 \text{ cm}^{-1}$. We thus find good agreement between the vDOS and experimentally obtained Raman spectra for Sm^{3+} in LiCl-KCl within normal tolerance of the differences inherent to the two spectra.

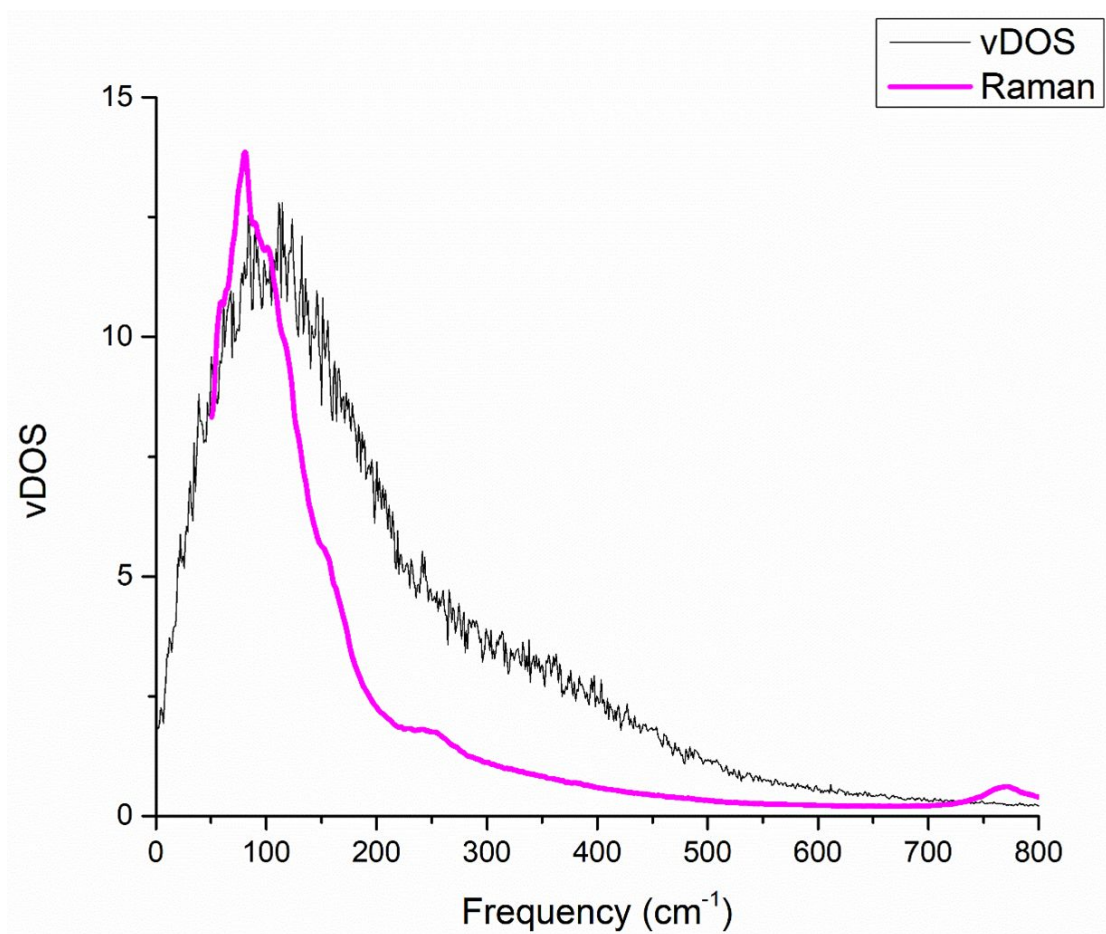


Fig. 6 – Vibrational DOS (black) and experimental Raman spectra (red) of 7.8 wt. % Eu^{3+} (EuCl_6^{3-}) in LiCl-KCl at 500°C. The computational vibrational DOS is redshifted by $\sim 125 \text{ cm}^{-1}$ compared to the experimental Raman spectrum (intensity of Raman scaled for comparison).

Similarly, we find good agreement between the vDOS and Raman spectrum obtained for low wt.% Eu^{3+} in LiCl-KCl (Fig. 6), further validating the 2PT computational approach for determining the vDOS of a molten salt. Similar to Sm^{3+} , the Eu^{3+} Raman spectra consists of a primary peak at $\sim 90 \text{ cm}^{-1}$ and a secondary shoulder peak at $\sim 250 \text{ cm}^{-1}$; distinctly Eu^{3+} also contains a Raman spectrum feature at $\sim 760 \text{ cm}^{-1}$ which is not found in Sm^{3+} . The primary peak in the Eu^{3+} Raman spectra is considerably more complex than that of Sm^{3+} , with multiple shoulder features that are likewise seen in the vDOS as three distinct characteristics in the $\sim 60 \text{ cm}^{-1}$ - $\sim 130 \text{ cm}^{-1}$ range ($\sim 64 \text{ cm}^{-1}$, $\sim 88 \text{ cm}^{-1}$ and $\sim 125 \text{ cm}^{-1}$, respectively). The feature at ~ 760

cm^{-1} is not significantly present in the vDOS. The overall vDOS characterization is similar to that of Sm^{3+} in other regards and has similar agreement with the Raman spectrum as previously described for that species. An overlay of the two vDOS is shown in Fig. S4 to illustrate these differences and similarities between the two lanthanides in LiCl-KCl. We thus note that the primary difference in the computational vDOS obtained is the significant difference between the primary feature, while other features in the vDOS are less clearly differentiated between the two species.

CONCLUSIONS

The coordination behavior and physical properties of various trivalent lanthanide species (Sm^{3+} , Eu^{3+} , Ce^{3+}) were investigated computationally using QM-MD and 2PT analysis. All species were observed to adopt an octahedral structure typical of trivalent species (LaCl_6^{3-}), with Ce^{3+} having significant fluctuations between six-and-seven coordinated across the equilibrium molecular dynamics. This behavior was elucidated through structural analysis, in which Ce^{3+} was found to have closer Cl distances than the other two lanthanide species studied. In the case of both Sm^{3+} and Eu^{3+} the octahedral coordination was found to be more consistent in the MD, with both species having similar LiCl/KCl coordination numbers indicating no such clustering of Cl to influence this type of six-to-seven coordinated fluctuation in the chlorocomplexes.

Physical properties of the three species such as density, heat capacity, fluidicity, and diffusivity (calculated from 2PT analysis of the system) were predicted computationally. The density of both the pure eutectic system and Ce^{3+} in LiCl-KCl eutectic based on the equilibrium volume were found to have excellent agreement with experimental results, lending validity to the computational method. The specific heat (C_v) of each lanthanide salt composition was slightly increased compared to pure eutectic LiCl-KCl, while both diffusivity and fluidicity were decreased for the lanthanide compositions relative to the pure salt. The fluidicity and diffusivity of low wt.% (6.9% CeCl_3) Ce^{3+} in LiCl-KCl was found to deviate significantly from the other two trivalent lanthanide species investigated in this work; this is likely due to increased Ce-Cl attraction causing lowered Li and K coordination and increased Ce coordination which inhibits the motion in the simulated system. This behavior is mitigated by increasing the wt. % of Ce present, as the 19.4 wt. % system for CeCl_3 is found to have similar diffusivity compared to the low wt. % systems of Eu and Sm in LiCl-KCl eutectic. Increasing the amount of Ce in the system decreases the stronger Ce-Cl interaction found in LiCl-KCl due to repulsive effects between the local negative charge on the chlorocomplexes and the negatively-charged Cl species in the system.

The Raman spectra for two species (Sm^{3+} and Eu^{3+}) were obtained using laser excitation methods and compared with the vDOS obtained from the 2PT analysis. Good agreement between the computationally obtained vDOS and the experimentally obtained Raman spectra was found, with the normal intensity difference between the two due to Raman mode selection criteria present. Primary Raman peaks at $\sim 90 \text{ cm}^{-1}$ and secondary peaks at $\sim 250 \text{ cm}^{-1}$ were found for both species and similarly represented in the vDOS for each; a tertiary feature in the Raman spectra only found for Eu^{3+} at $\sim 760 \text{ cm}^{-1}$. In both cases the Raman spectra was in good agreement with previous findings for lanthanide species in LiCl-KCl media.

These findings provide significant insight into the behavior of trivalent lanthanides in eutectic LiCl-KCl, and the excellent agreement between the computational methods proposed here and experimental findings indicates the suitability of this computational approach to evaluate the behavior of various lanthanide species in other molten salt media.

ELECTRONIC SUPPLEMENTARY INFORMATION

Fig S1 – Single Ce coordination

Fig S2 – 19.4 wt.% Ce RDF/CN

Fig S3 – ν DOS of LiCl-KCl eutectic at 500°C

Fig S4 – ν DOS of Sm^{3+} and Eu^{3+} in LiCl-KCL eutectic overlay

AUTHORS CONTRIBUTIONS

QA designed the strategy of this work. JF and QA performed QM calculations. JZ performed 2PT calculations. JM and DC performed Raman experiments. All authors wrote the paper.

CORRESPONDING AUTHOR

* E-mail: qia@unr.edu (Qi An)

ORCID

Jon Fuller: 0000-0003-1233-7842

Jeremy Moon: 0000-0001-5326-7882

Jing Zhang: 0000-0001-9122-2669

Dev Chidambaram: 0000-0002-3918-3559

Qi An: 0000-0003-4838-6232

CONFLICTS OF INTEREST

The authors declare no competing financial interest.

ACKNOWLEDGEMENTS

This research is being performed using funding received from the DOE Office of Nuclear Energy's, Nuclear Energy University Program under grant No. DE-NE0008889.

REFERENCES

(1) S. X. Li, Anodic Process of Electrorefining Spent Nuclear Fuel in Molten LiCl-KCl-UCl₃/Cd System, *ECS Proc. Vol.*, 2002, **19**, 541-552.

- (2) T. J. Harrison, D. E. Holcomb, G. F. Flagman, B. W. Patton, J. C. Gehin, and R. L. Howard, Fast Spectrum Molten Salt Reactor Options, ORNL Technical Report, 2011, Web, <https://doi.org/10.2172/1018987>.
- (3) J. Zhang, Electrochemistry of Actinides and Fission Products in Molten Salts - Data Review, *J. Nucl. Mater.*, 2014, **447**, 271–284.
- (4) Y. A. Barbanel', V. V. Kolin, V. P. Kotlin, and A. A. Lumpov, Coordination Chemistry of Actinides in Molten Salts, *J. Radioanal. Nucl. Chem. Artic.*, 1990, **143**, 167–179.
- (5) J. Song, S. Shi, X. Li, and L. Yan, First-Principles Molecular Dynamics Modeling of UCl_3 in LiCl-KCl Eutectic, *J. Mol. Liq.*, 2017, **234**, 279-286.
- (6) R. Hoover, M. Shaltry, S. Martin, K. Sridharan, and S. Phongikaroon, Electrochemical Studies and Analysis of 1-10 wt% UCl_3 Concentrations in Molten LiCl-KCL Eutectic, *J. Nuc. Mat.*, 2014, **452**, 389-396.
- (7) D. Yoon, and S. Phongikaroon, Electrochemical and Thermodynamic Properties of UCl_3 in LiCl-KCl Eutectic Salt System and LiCl-KCl-GdCl₃ system, *J. Elec. Soc.*, 2017, **164**, E217.
- (8) J. Jones, and E. Jensen, Radiations from Cerium-141, *Phys. Rev.*, 1955, **97**, 1031-1033.
- (9) K. Aitken, D. Littler, E. Lockette and G. Palmer, The Pile-Neutron Absorption Cross-Section of Samarium-149, *J. Nuc. Energy*, 1957, **4**, 33-37.
- (10) D. E. Mahagin, Fast Reactor Neutron Absorber Materials, *Am. Ceram. Soc.*, 1979, Available online via OSTI: <https://www.osti.gov/servlets/purl/6200971>.
- (11) T. Fujii, T. Nagai, A. Uehara, and H. Yamana, Electronic Absorption Spectra of Lanthanides in a Molten Chloride – III. Absorption Characteristics of Trivalent Samarium, Dysprosium, Holmium and Erbium in Various Molten Chlorides. *J. Alloys Compd.* 2007, **441**, 10-13.
- (12) K. Fukasawa, A. Uehara, T. Nagai, N. Sato, T. Fujii, and H. Yamana, Thermodynamic Properties of Trivalent Lanthanide and Actinide Ions in Molten Mixtures of LiCl-KCl, *J. Nuc. Mat.*, 2012, **424**, 17-22.
- (13) T-J. Kim, Y-K. Jeong, J-G. Kang, Y. Jung, D-H. Ahn and H-S. Lee, In Situ Analysis for Spontaneous Reduction of Eu^{3+} in LiCl Pyroprocessing Media at 923 K, *J. Radioanal. Nucl. Chem.*, 2010, **286**, 283-286.
- (14) Y-Z. Cho, G-H. Park, H-C. Yang, D-S. Han, H-S Lee and I-T. Kim, Minimization of Eutectic Salt Waste from Pyroprocessing by Oxidative Precipitation of Lanthanides, *J. Nucl. Sci. Technol.* 2009, **46**, 1004-1011.
- (15) J. P. Perdew, K. Burke, and M. Ernzerhof, Generalized Gradient Approximation Made Simple, *Phys. Rev. Lett.*, 1996, **77**, 3865–3868.
- (16) J. P. Perdew, K. Burke, and M. Ernzerhof, Erratum: Generalized gradient approximation made simple, *Phys. Rev. Lett.*, 1997, **78**, 1396

- (17) S. Grimme, J. Antony, S. Ehrlich, and S. Krieg, A Consistent and Accurate ab Initio Parametrization of Density Functional Dispersion Correction (dft-d) for the 94 Elements H-Pu', *J. Chem. Phys.* 2010, **132**, 154104.
- (18) G. Kresse, and J. Hafner, Ab Initio Molecular Dynamics for Liquid Metals, *Phys. Rev. B*, 1993, **47**, 558-561.
- (19) G. Kresse, and J. Hafner, Ab Initio Molecular-Dynamics Simulation of the Liquid-Metal–Amorphous-Semiconductor Transition in Germanium, *Phys. Rev. B*, 1994, **49**, 14251-14269.
- (20) G. Kresse, and J. Furthmüller, Efficiency of Ab-Initio Total Energy Calculations for Metals and Semiconductors Using a Plane-Wave Basis Set, *Comput. Mater. Sci.*, 1996, **6**, 15-50.
- (21) J. G. Kirkwood, and E. M. Boggs, The Radial Distribution Function in Liquids, *J. Chem. Phys.* 1942, **10**, 394-402.
- (22) S-T. Lin, P. K. Maiti, and W. A. Goddard III, Two-Phase Thermodynamic Model for Efficient and Accurate Absolute Entropy of Water from Molecular Dynamics Simulations, *J. Phys. Chem. B*, 2010, **114**, 8191-8198.
- (23) T. A. Pascal, S-T. Lin, and W. A. Goddard III, Thermodynamics of Liquids: Standard Molar Entropies and Heat Capacities of Common Solvents from 2PT Molecular Dynamics, *Phys. Chem. Chem. Phys.*, 2011, **13**, 169-181.
- (24) J. Wang, B. Chakraborty, and J. Eapen, Absolute Thermodynamic Properties of Molten Salts using the Two-Phase Thermodynamic (2PT) Superpositioning Method, *Phys. Chem. Chem. Phys.*, 2014, **16**, 3062-3069.
- (25) V. J. Singh, C. D. Bruneau, and D. Chidambaram, In situ Raman Spectroscopy of Samarium Ions in Molten LiCl-KCl Eutectic, *ECSSarXiv*, 2019, Web, <https://doi.org/10.1149/osf.io/qpsr3>.
- (26) K. Fukasawa, A. Uehara, T. Nagai, N. Sato, T. Fujii and H. Yamana, Thermodynamic Properties of Trivalent Lanthanide and Actinide Ions in Molten Mixtures of LiCl and KCl, *J. Nuc. Mat.*, 2012, **424**, 17-22.
- (27) C. Kwon, S. H. Noh, H. Chun, I. S. Hwang, and B. Han, First Principles Computational Studies of Spontaneous Reduction Reaction of Eu(III) in Eutectic LiCl-KCl Molten Salt, *Int. J. Energy Res.*, 2018, **42**, 2757-2765.
- (28) H. Matsuura, S. Watanabe, T. Sakamoto, T. Kanuma, K. Naoi, M. Hachio, N. Kitamura, H. Akatsuka, A. K. Adya, T. Honma, T. Uruga, and N. Umesaki, Short-Range Structure of Molten CeCl₃ and NdCl₃ Determined by XAFS. *J. Alloys Compd.*, **2006**, 408-412, 80-83.
- (29) T. Jiang, N. Wang, C-M. Cheng, S-M. Peng, and L-M. Yan, Molecular Dynamics Simulation on the Structure and Thermodynamics of Molten LiCl-KCl-CeCl₃. *Acta Phys.-Chim. Sin.*, **2016**, 32, 647-655.
- (30) S. Wang, S. Xiao, W. Hu and H. Deng, Effect of MCl₃ (M=La, U or Sc) Component on the Local Structures and Transport Properties of LiCl-KCl-MCl₃ Eutectic: A Molecular Dynamics Study, *Electrochem. Acta*, 2019, **20**, 366-376.

- (31) K. Sridharan, S. Martin, M. Mohammadian, J. Sager, T. Allen, and M. Simpson, Thermal Properties of LiCl-KCl Molten Salt for Nuclear Waste Separation. *Trans. Am. Nucl. Soc.* 2012, **106**, 1240–1241.
- (32) S. Malola, H. Hakkinen, and P. Koskinen, Comparison of Raman Spectra and Vibrational Density of States between Graphene Nanoribbons with Different Edges. *Eur. Phys. J.* **2009**, *52*, 71-74.
- (33) E. Schellkes, X. Hong, M. Holz, U. Huniar, R. Ahlrichs, and W. Freyland, High temperature ^{93}Nb NMR and Raman spectroscopic investigation of the structure and dynamics of solid and liquid NbCl_5 -alkali chloride solutions. *Phys. Chem. Chem. Phys.* 2003, **5**, 5536-5543.
- (34) S. Malola, H. Hakkinen, and P. Koskinen, Comparison of Raman spectra and vibrational density of states between graphene nanoribbons with different edges. *Eur. Phys. J.* 2009, **52**, 71-74.
- (35) P. Umari, and A. Pasquarello, First-Principles Analysis of the Raman Spectrum of Vitreous Silica: Comparison with the Vibrational Density of States. *J. Phys: Con. Matter*, **2003**, *15*, 1547.
- (36) R. Shuker, and R. W. Gammon, Raman-Scattering Selection Rule Breaking and the Density of States in Amorphous Materials. *Phys. Rev. Lett.*, **1970**, *25*, 222-225.